NANO LETTERS

pubs.acs.org/NanoLett Letter

Mechanistic Insights into Superlattice Transformation at a Single Nanocrystal Level Using Nanobeam Electron Diffraction

Jessica Cimada daSilva, Michelle A. Smeaton, Tyler A. Dunbar, Yuanze Xu, Daniel M. Balazs, Lena F. Kourkoutis, and Tobias Hanrath*

Cite This: *Nano Lett.* 2020, 20, 5267−5274 Read Online

ACCESS | Metrics & More | Article Recommendations | Supporting Information

ABSTRACT: Understanding the mechanism and ultimately directing nanocrystal (NC) superlattice assembly and attachment have important implications on future advances in this emerging field. Here, we use 4D-STEM to investigate a monolayer of PbS NCs at various stages of the transformation from a hexatic assembly to a nonconnected square-like superlattice over large fields of view. Maps of nanobeam electron diffraction patterns acquired with an electron microscope pixel array detector (EMPAD) offer unprecedented detail into the 3D crystallographic alignment of the polyhedral NCs. Our analysis reveals that superlattice transformation is dominated by translation of prealigned NCs strongly coupled along the $<11n>_{AL}$ direction and occurs stochastically and gradually throughout single grains. We validate the generality of the proposed mechanism by examining the structure of analogous PbSe NC assemblies using conventional transmission electron microscopy and selected area electron diffraction. The experimental results presented here provide new mechanistic insights into NC self-assembly and oriented attachment.

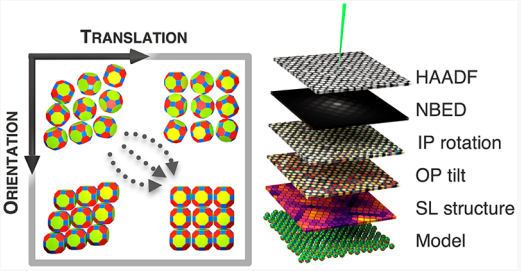

KEYWORDS: *Nanocrystals, self-assembly, oriented attachment, superlattice, 4D-STEM, EMPAD*

INTRODUCTION

The prospect of creating and studying programmable materials formed by the directed assembly and attachment of colloidal nanocrystals (NCs) has inspired and intrigued scientists for the past two decades.[1−3] Access to NC building blocks with precisely controlled size, shape, and composition and advances in synthetic control over inter-NC coupling have created a fertile opportunity space for creating programmable materials.[4−7] Semiconducting lead chalcogenide NCs and their assemblies present a particularly interesting model system by virtue of the strong quantum confinement effects and the availability of colloidal NC building blocks with well-defined size and polyhedral faceting.[8,9] Recent advances to create epitaxially connected superstructures have provided access to superlattices in which neighboring NCs are held in precise registry within the (para)crystal and are strongly coupled electronically.[10−12]

Atomistic tight binding calculations of such superlattices forecast a rich electronic structure with experimentally accessible bandwidths.[13−15] Currently available superlattices lack the fidelity to test many of the predicted characteristics emerging from long-range charge delocalization.[10,12,16] Future progress toward creating test structures in which the predicted emerging electronic properties can be probed and exploited is predicated on better understanding of and control over the coupled subsequence of NC assembly and attachment. What is astounding, and not yet well understood, is how the irreversible attachment of ~10^5 NCs in an imperfect preassembly is orchestrated to yield the formation of micrometer-sized epitaxially connected superlattice grains.

The transformation of an unconnected hexatic assembly into an epitaxially connected square superlattice involves a complex choreography of translating and orienting the constituent NCs. Some of the possible transformation pathways are illustrated in Figure 1. In the case of 3D assemblies, Abelson et al.[17] recently reported that a distorted body-centered cubic assembly can transform into a distorted simple cubic epitaxially connected quantum dot solid via a topotactical transformation pathway. In the case of 2D assemblies, Geuchies et al.[18] proposed a model for the hexatic-to-square superlattice transformation of PbSe monolayers. In these studies, the transformation pathway was inferred from selected area electron diffraction (SAED) at single grain level, combined with X-ray scattering experiments at micrometer length scales. Fundamental limitations in real and reciprocal space correlation limit the ability to unambiguously determine the fine structure of NCs positional and in-plane and out-of-plane orientational arrangement throughout the transformation (Figure S5). Wang et al.[19] investigated the superlattice transformation of PbSe mono-

Received: April 12, 2020
Revised: June 2, 2020
Published: June 2, 2020

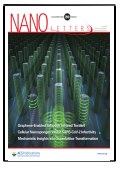

https://dx.doi.org/10.1021/acs.nanolett.0c01579
Nano Lett. 2020, 20, 5267−5274

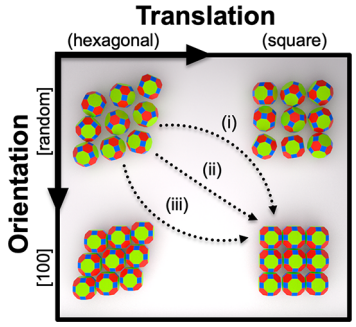

Figure 1. Illustration of transformation pathways by which monolayer NC superlattices may form through translational and orientational alignment. Whether the transformation pathway involves subsequent translation followed by rotation (path (i)) or vice versa (path (iii)), or by a concerted change of NC position and orientation (path (ii)), has not been known.

layers using high-resolution real-time imaging with liquid-phase TEM. This technique provides rich details about NC−NC interactions and the dynamics of NC attachment; however, limitations arise regarding transformation of ordered assemblies on a fluid−fluid interface.

Recent advances in electron microscopy, in specific, the introduction of pixelated STEM detectors which have enabled new 4D-STEM approaches,[20,21] provide a unique opportunity to resolve this challenge. Detectors with fast readout, high dynamic range, and high sensitivity, such as the electron microscope pixel-array detector (EMPAD),[20] enable the acquisition of nanobeam electron diffraction (NBED) maps pixel by pixel with a nanometer-sized electron probe. NBED provides detailed structural information, such as the degree of in-plane and out-of-plane crystallographic tilt of individual NCs. In this work, we precisely determined the position and crystallographic orientation of single NCs within superlattices with "transient regions" containing hexatic and square-like structures. For simplicity, we define the initial hexatic superlattice as HX and the final square-like superlattice as SQ. We note that the HX and SQ structures shown in Figure 1 are the end points of the transformation. Here, we investigate the intermediate states of this transformation. New mechanistic insights gained from this detailed structural analysis provide important guidance to future efforts to better understand and control NC superlattice transformations.

RESULTS AND DISCUSSION

We characterized monolayers of PbS NCs assembled at an ethylene glycol (EG) interface. Experimental details on the NC synthesis and self-assembly are provided in the Supporting Information.[10,22] The HX-to-SQ superlattice transformation is initiated by displacing oleate ligands bound to the surface of the NCs with a chemical trigger in a way that transient structures between HX and SQ domains are obtained. The gradual removal of surface-bound ligands "deprotects" the NCs, induces the superlattice transformation, and enables proximate NCs to attach via mutually exposed facets.

We determined the precise position and crystallographic orientation of each NC in the superlattice via a 4D-STEM technique using the EMPAD (Figure 2a).[20] An ∼2 nm sized probe scans over the sample and generates a NBED pattern at each scan position. We identified the position and obtained an averaged NBED pattern for each NC in the field of view (Figure 2b and c). We determined the in-plane (IP) and out-of-plane (OP) AL tilt angles by comparing single-particle NBED patterns from each NC to a series of simulated NBED patterns[23] (see the Methods section in the SI for details). Figure 2d shows examples of matching experimental and simulated NBED patterns for NCs with 0°, ∼5°, and ∼15° OP tilt angle. The IP and OP tilt angles of the polyhedral NCs are quantified as illustrated in Figure 2e. The IP tilt angle is defined by the orientation of the $(200)_{AL}$ diffraction spot in the range of 0−90°, and the OP tilt angles over directions x and y are defined by $OP_x \| IP$ and $OP_y \perp OP_x$.

We investigated regions predominantly HX (Figure 2f−i) and predominantly SQ (Figure 2j−m). A virtual annular dark field (ADF) image of the superlattice was reconstructed from the scanning diffraction data set (Figure 2f and j). The average NBED pattern over the entire field of view is shown in the *inset*. Bragg spots (instead of rings) in the average NBED indicates AL alignment over the entire field of view and suggests that each region lies within a single domain.

We quantitatively analyzed the local superlattice structure by calculating a local bond order parameter that corresponds to the degree of local 6-fold symmetry (Ψ_6) and 4-fold symmetry (Ψ_4) using an algorithm developed in-house.[11] High-angle annular dark field (HAADF) images obtained with a subångström electron probe (Figure S6) provide a more accurate description of the NCs' position and local structure, compared to the virtual ADF images, and were therefore used to calculate the Ψ_6 and Ψ_4 parameters. Figure 2g and k show Voronoi diagrams with the local superlattice structure and Ψ_4 normalized between 0 and 1, where 0 and 1 corresponds to the most hexagonal and square regions within the data frame, respectively (see Figure S6 for Ψ_6 diagrams).

The mechanism by which NC superlattices transform their symmetry structure has been subject to ongoing debate.[18,24] Previously, the presence of well-defined grain boundaries between unconnected (body-centered cubic) and connected (simple cubic) domains in multilayered superlattices suggested that a coherent phase transformation starting from grain boundaries may occur.[24] In the case of monolayer superlattices, the presence of multiple HX-to-SQ transient regions suggests that the superlattice transformation occurs gradually throughout single grains. The stochastic emergence of multiple transformation regions appears to result from the inherent distribution of ligand coverage in the NC ensemble.[25] We note that the concentration of the chemical trigger is effectively constant at the length scales probed in the TEM sample (10^{-7} m). Additional HAADF-STEM images further corroborate that the superlattice structure transformation occurs within superlattice grains (Figure S7). The transformation process is more analogous to bulk diffusionless transformations in atomic crystals (e.g., martensitic transformation) than to the previously reported domain boundary propagation mechanism in multilayered superlattices.[24] This observation indicates that the grain boundaries form in the initial drying and assembly process rather than in the subsequent transformation process.

The AL alignment evident in the average NBED data (Figure 2f, j *inset*) is remarkable given the variation in translational order in the transient regions. This AL alignment corroborates SAED and *in situ* X-ray scattering experiments from Geuchies et al.[18] which showed preferential IP orientation in both the HX and SQ phases. Whereas X-ray scattering experiments provide time-resolved insights into the transformation,[18] it is important to note that scattering signatures reflect an average over relatively large areas which

https://dx.doi.org/10.1021/acs.nanolett.0c01579
Nano Lett. 2020, 20, 5267−5274

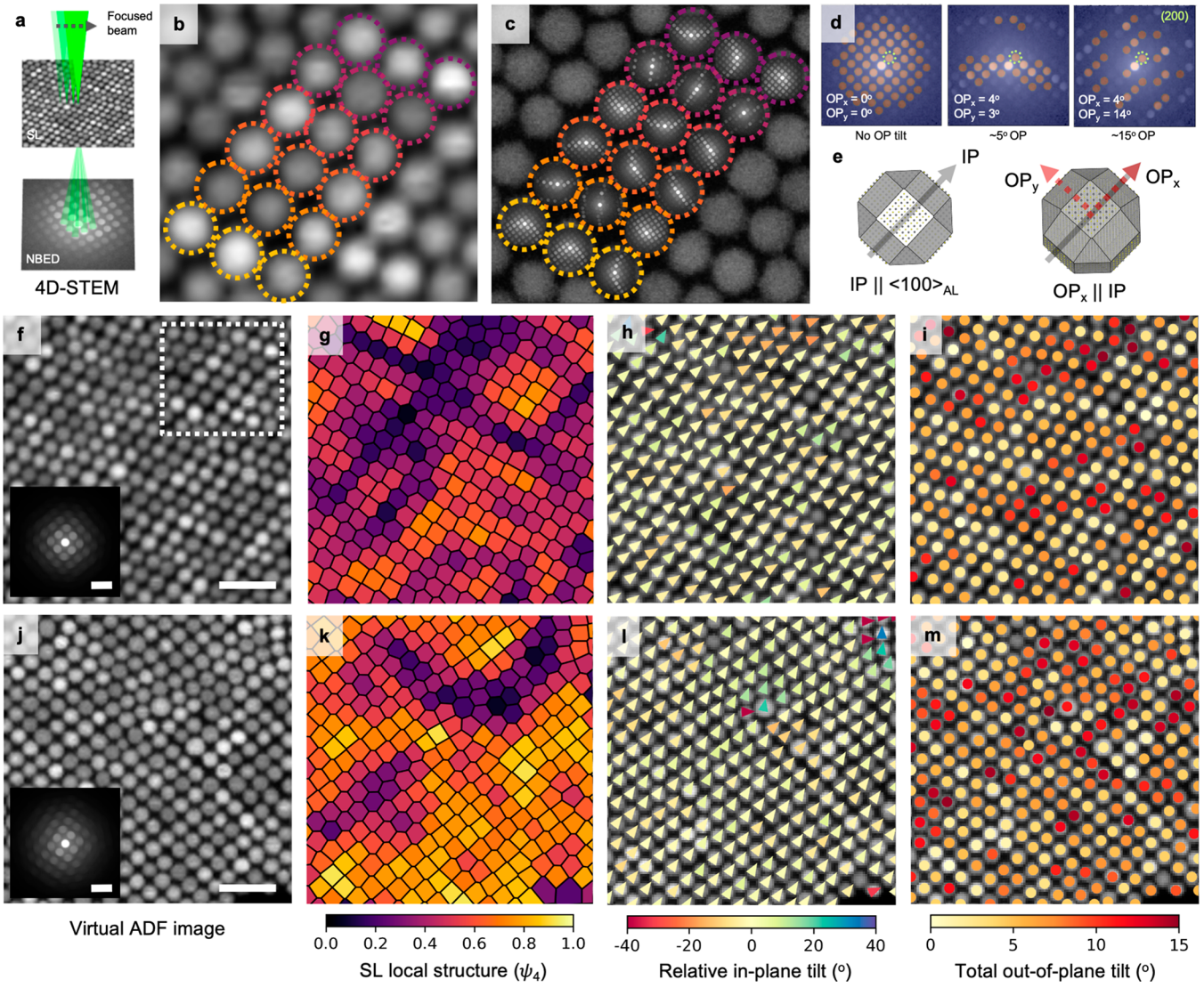

Figure 2. 4D-STEM characterization of a monolayer of ~7 nm PbS truncated cuboctahedron NCs. (a) Illustration of 4D-STEM: A focused beam scans over the sample and generates a NBED pattern at each scan position. (b) Eighteen NCs within a virtual annular dark field image of the region indicated by the dotted white box in (f). (c) Nanobeam electron diffraction patterns obtained with the EMPAD detector overlaid with a HAADF STEM image of the same region. (d) Series of electron diffraction patterns matched to simulated patterns for 0°, ~5°, and ~15° total OP tilt. The IP tilt angle is defined by the $(200)_{AL}$ spot in the electron diffraction pattern identified by the dotted green circles. (e) Illustration of IP angle defined by the orientation of the $\{100\}_{AL}$ facet of the NC and OP tilt angles over directions *x* and *y*, where OP_x is parallel to the IP angle. (f–i) Predominantly HX sample region (288 NCs) and (j–m) predominantly SQ sample region (295 NCs). (f, j) Virtual annular dark field image with size set to 128 × 128 pixels, resulting in the collection of 16384 patterns per data frame. The *inset* corresponding to the average NBED over the whole scanned region shows remarkable AL alignment of NCs within the field of view. (g, k) Voronoi diagram with cells colored according to the local 4-fold symmetry Ψ_4, normalized between 0 and 1, showing the presence of many HX-to-SQ transition regions with small 4-fold symmetry domains in the predominantly HX region (g) and large 4-fold symmetry domains in the predominantly SQ region (k). (h, l) Relative IP orientation of the NCs' $\{100\}_{AL}$ facet normalized by the average IP angle of all NCs within the field of view: 39° and 56° for the predominantly HX and SQ regions with a 6° and 5° standard deviation, respectively. (i, m) Total OP tilt of the NCs revealing the diversity in OP orientation from 0° to 15°. Scale bar: (f, j) Virtual ADF image 20 nm; NBED 3.4 nm^{-1}.

can obscure important details about the transformation and the "trajectory" of constituent NCs (Figure S5). What was not yet known is the translational and orientational trajectory of individual NCs throughout the phase transition in the superlattice transformation, which can now be accessed by single NC NBED using 4D-STEM.

We developed a data processing algorithm that allowed us to determine the crystallographic orientation for 95% of the NCs in the scanned region. Figure 2h and l show detailed relative IP orientation of the NCs' $\{100\}_{AL}$ facets normalized by the average IP angle. The detailed statistical distribution of IP angles is given in Figure S8. Most NCs within the superlattice grain have a preferential orientation regardless of the local superlattice structure (~95% of NCs have less than 10° off the average tilt). This result suggests that the NCs' preferred IP AL alignment relative to each other is defined at early stages of the self-assembly process, in agreement with kinetic studies on the self-assembly of PbS NCs by Weidman and co-workers.[26] Since the NCs' IP orientation remains nearly unchanged throughout the transformation, we conclude that the HX-to-SQ superlattice transformation is dominated by translation of prealigned NCs. We note that a few NCs present larger IP

https://dx.doi.org/10.1021/acs.nanolett.0c01579
Nano Lett. 2020, 20, 5267–5274

misalignment due to local defects such as cracks in the superlattice, presence of nonuniform NC size distribution, or neighboring grains, as in the case of the NCs on the top-right of Figure 2l (Figure S7). The magnitude of global OP tilt angle for each NC reveals a diverse distribution in the 0° to 15° range (Figure 2i and m). The total OP tilt of NCs in the HX and SQ regions have similar distributions with no preferential tilt direction away from 0° and are oriented with their $<100>_{AL}$ axes close to surface normal, where 85% of NCs have an OP global tilt ranging from 0° to 10° and 15% of NCs have larger OP tilt angles of up to 15° (Figure S9).

Access to the complete description of the NC superlattice presents an opportunity to examine the relationship between local superlattice structure (Ψ_6 and Ψ_4) and NC orientation. Figure 3a and b show the IP angle distribution normalized by the average IP angle in the ±20° range for the NCs in the HX and SQ regions versus Ψ_4 (see Figure S10 for IP versus Ψ_6). This relationship reveals that NCs in HX regions ($\Psi_4 < 0.5$) have broader IP angle distributions compared to NCs in SQ ($\Psi_4 \geq 0.5$), which indicates that during the HX-to-SQ superlattice structure transformation, NCs continue to refine the AL alignment and sharpen the IP angle distribution (Figure 3c).

To visualize the position and orientation of each NC in the HX-to-SQ transition region, we translated the 4D-STEM data into a 3D model (Figure 4a). We provide an animation showing a 3D reconstruction of the NCs in the field of view (Movie S1). Figure 4b shows the NC model overlaid with the local structure of a HX-to-SQ transition region, where the orientation of the $<11n>_{AL}$ is correlated to $<11>_{SL}$ (Movie S2). A closer look at a HX region reveals a nearly perfect $<11n>_{AL}$ directional alignment along one of the HX superlattice symmetry axes (Figure 4c). Interestingly, given the centrosymmetric structure of the rock-salt NCs, the preferred alignment along the $<11n>_{AL}$ suggests that the superlattice structure transformation involves a symmetry breaking compared to an idealized hexagonal close-packed layer with randomly oriented NCs (Figure S12).

We interpret the preferred alignment of proximate $\{11n\}_{AL}$ facets as an indication that the residual ligand density on $\{11n\}_{AL}$ facets play an important role as directing agents to drive the stability of the preformed HX assembly through ligand−ligand interactions. Notably, the strong NC correlation along the $<11n>_{AL}$ direction is present prior, during, and after superlattice transformation, and the NC AL orientation in the prealigned HX structure determines the orientation of the final SQ superlattice. Previous reports about the relative ligand coverage on $\{100\}_{AL}$, $\{110\}_{AL}$, and $\{111\}_{AL}$ facets of polyhedral lead salt NCs pointed toward a higher ligand coverage on $\{111\}_{AL}$ facets relative to $\{110\}_{AL}$ and $\{100\}_{AL}$.[8,17] Preferred interactions between $\{111\}_{AL}$ facets have been previously reported for unconnected 2D and 3D body-centered tetragonal PbS superlattices.[27,28] Oleic acid has also been reported to induce IP AL alignment with long-range order in 2D ZnS polyhedral superlattices.[29] We interpret the preferred alignment along the $<11n>_{AL}$ direction in terms of an orientation driven by preferred organization of residual ligands on $\{11n\}_{AL}$ facets to minimize the superlattice free energy.[30,31] Further ligand displacement on $\{11n\}_{AL}$ facets will weaken ligand−ligand interactions, and the high surface energy of deprotected $\{100\}_{AL}$ facets induces translation and attachment of the NCs, increasing AL order.[19]

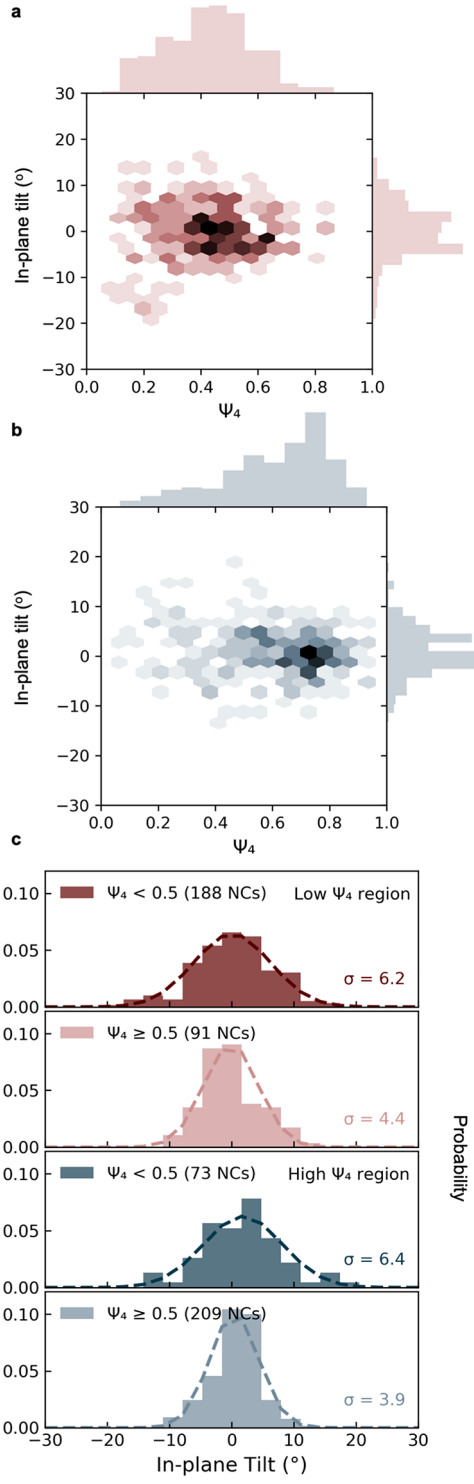

Figure 3. (a, b) IP tilt angles correlated with local superlattice structure (Ψ_4) for the predominantly HX and SQ regions, respectively. (c) Probability density function of IP tilt angles for low and high Ψ_4 number showing narrower angle distribution for $\Psi_4 \geq 0.5$ compared to $\Psi_4 < 0.5$, indicating fine IP AL alignment as the superlattice transforms from HX-to-SQ structure. Our conclusion is robust relative to the Ψ_4 threshold values (Figure S11).

Based on the structural analysis discussed above, we conclude that the transformation mechanism is one in which the NC building blocks first orient to achieve $<100>_{AL}$ axes normal to the plane. Figure S9 shows that 85% of NCs have

https://dx.doi.org/10.1021/acs.nanolett.0c01579
Nano Lett. 2020, 20, 5267−5274

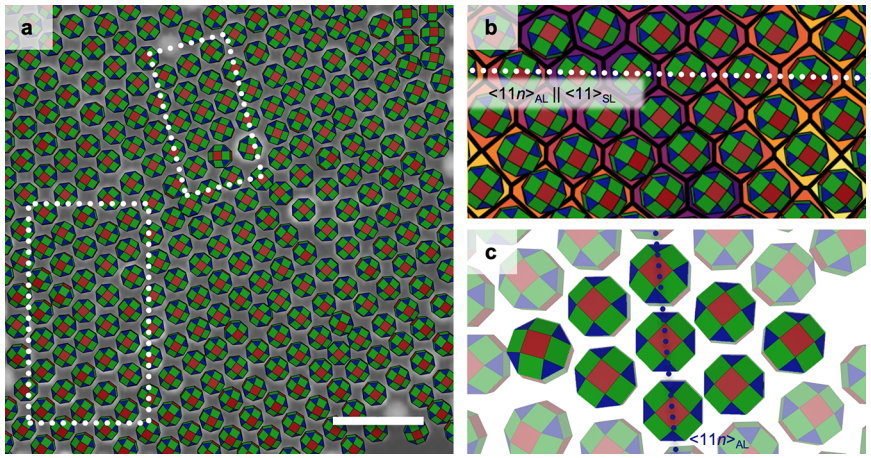

Figure 4. Rich information content available from the EMPAD data allows us to create a detailed 3D reconstruction model based on the assumption that the NCs are within the plane of the superlattice. (a) Superlattice model reflecting NC orientation across the field of view of the predominantly SQ region. This model illustrates NCs with uniform size and shape for simplicity. We note that we could not unambiguously identify the orientation of 4 out of 295 NCs in this field of view because of their high degree of OP tilt (above 15°). (b) Detailed NC orientation (model) and superlattice local structure (Voronoi diagram Ψ_4) showing correlation along the $<11n>_{AL}$ and $<11>_{SL}$ direction across the transient region. (c) NC model of HX region reveals a nearly perfect $<11n>_{AL}$ alignment. Scale bar: (a) 20 nm.

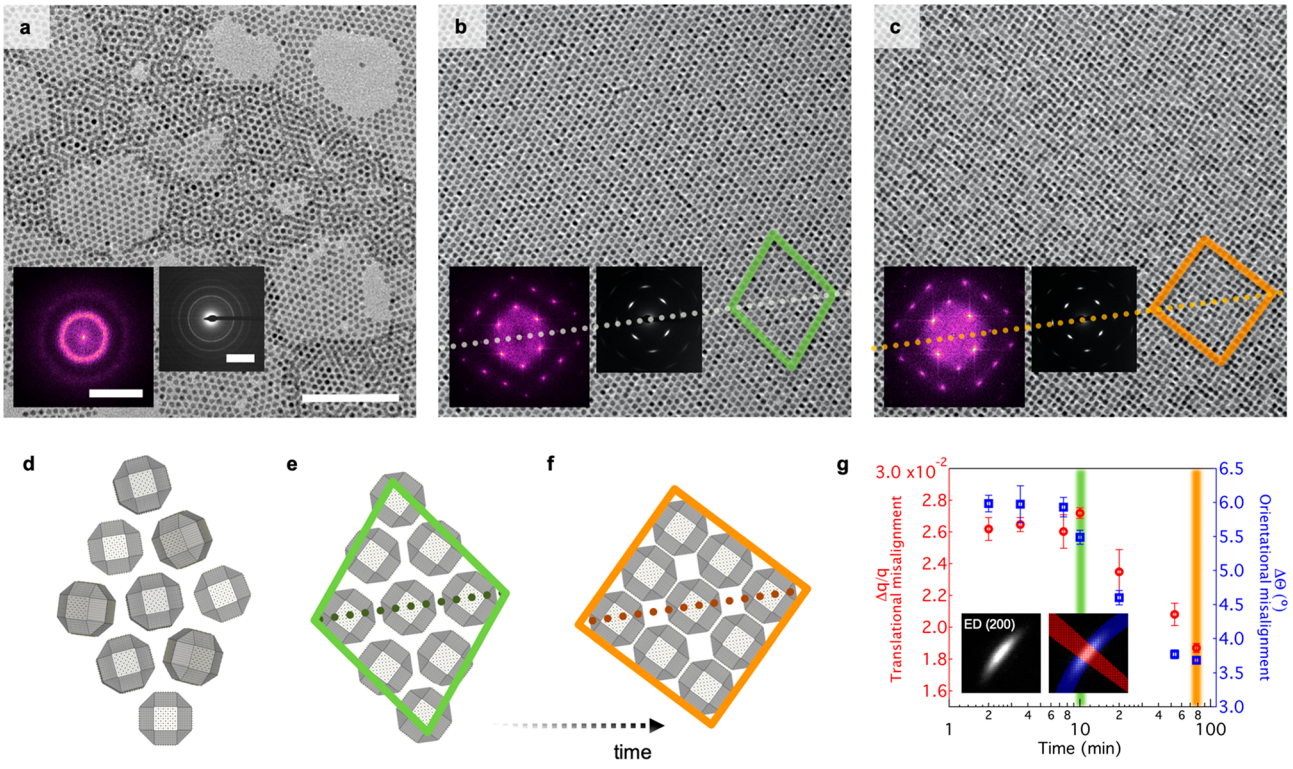

Figure 5. Series of TEM, FFT, and SAED images and a schematic of the mechanism for superlattice transformation. (a, d) The initial hexagonal structure with randomly oriented NCs obtained by drop casting NCs onto a solid substrate (TEM grid). This structure was not observed experimentally on NCs assembled on an EG subphase. (b, e) HX and (c, f) SQ structures obtained 10 and 78 min after NC injection on EG, respectively, in which there is a correlated alignment along the $<11n>_{AL}$ and $<11>_{SL}$ direction. (g) Misalignment obtained from the azimuthal (shown in blue) and radial (shown in red) integration of the SAED $(200)_{AL}$ peaks shows a decrease in orientational and translational misalignment as the superlattice transforms from HX-to-SQ. Scale bar: (a–c) TEM 100 nm, SAED 4 nm^{-1}, FFT 0.3 nm^{-1}.

OP tilt angles below 10°. In addition, the NCs also align IP during early stages of the assembly formation on EG. Figure S8 shows that 95% of NCs have less than 10° degrees off the mean IP angle. Moreover, the average $<11n>_{AL}$ orientation of the NCs is parallel to the local $<11>_{SL}$ direction throughout the HX-to-SQ transformation. The initially oriented HX superlattice transforms toward the SQ phase through a collective IP translation that leads to increased overlap of the $\{100\}_{AL}$ facets. Concurrently with NC translation to the SQ phase, NCs undergo fine orientation alignment, further narrowing the IP angle distribution, after which NCs epitaxially attach. In context of the transformation pathways presented in Figure 1, the mechanism is closest to pathway iii.

https://dx.doi.org/10.1021/acs.nanolett.0c01579
Nano Lett. 2020, 20, 5267–5274

We note that no major changes have been observed in the SL structure and NC orientation due to superlattice transfer to the TEM grid or high vacuum in the TEM compared to in situ X-ray scattering experiments.[18] The extent to which the detailed SL structure is sensitive to the transfer process is currently unknown, but we expect that the SL structure is sufficiently robust. We note that the methods described here now offer the necessary precision to test this in future experiments.

To test the generality of the proposed mechanism, we examined the structure transformation of analogous PbSe NC superlattice formed at an EG surface via a slow ligand removal strategy (see Methods in the SI for more details) using the more conventional SAED technique. Figure 5a–c show a series of TEM images, their fast Fourier transform (FFT), and SAED patterns recorded in the same area, which informs the superlattice structure and the average AL orientation of the NCs. The dotted lines show the correlation along the $<11>_{SL}$ orientation in real space (TEM) and reciprocal space (FFT) and the $(220)_{AL}$ direction in reciprocal space (SAED).

Interactions between the NCs and the substrate play a critical role in the early stage orientational alignment of NCs. Drop-casting the colloidal NC solution on a carbon-coated TEM grid results in a hexagonal structure with randomly oriented NCs (Figure 5a). In contrast, depositing NCs on the surface of EG yields a superlattice characterized by NCs with preferred $<100>_{AL}$ axis (on average) normal to the plane of the interface and IP AL ordering in the HX and SQ phases (Figure 5b and c). Figure 5d–f show NC models that correlate with structures shown in Figure 5a–c.

To show the temporal evolution of the NC superlattice structure during the HX-to-SQ transformation, Figure 5b and c show the PbSe superlattice after 10 and 78 min of NC injection on EG, respectively. The correlation along the $<11n>_{AL}$ and $<11>_{SL}$ direction (dotted line) is preserved throughout the HX-to-SQ transformation, which further corroborates that the superlattice transformation is dominated by NC translation. We analyzed the $(200)_{AL}$ peaks in the SAED patterns obtained between 2 and 78 min after NC injection to investigate translational and orientational misalignment throughout the superlattice transformation (Figure 5g). The azimuthal and radial integration provide a measure of the degree of AL orientational and translational misalignment, respectively (see Figure S13 for more details). The width of the azimuthal peak decreases over time, indicating narrowed IP AL alignment distribution as NCs translate toward the SQ structure, in agreement with the conclusions from the EMPAD data (Figure 3c). As the superlattice undergoes the transformation, the width of the radial peak also decreases, meaning that the coherent domain size increases. These results show that the AL translational and IP orientational misalignment decrease during the HX-to-SQ superlattice transformation.

The preceding discussion illustrates that the complex interplay of polyhedral NC shape and facet-specific ligand coverage play a key role in guiding the structure transformation of the NC superlattice. Beyond the specific model system of truncated cuboctahedron lead salt NCs examined in this work, we expect that the general concept can also be translated to other systems. We note, however, that specific experimental aspects including the thermodynamic and kinetic conditions, NC size, shape, and ligand coverage need to be taken into consideration.

CONCLUSIONS

In summary, we present detailed structure analysis of PbS superlattice transient regions at the single NC level using scanning NBED with an EMPAD detector. This technique provides the precise position and a complete description of the crystallographic orientation of each NC in the field of view. We correlated NC orientation with a local bond order parameter to gain insights into the NC superlattice structure transformation pathway. We discovered that the transformation mechanism is dominated by translation of prealigned NCs. Notably, a strong correlation along the $<11n>_{AL}$ and $<11>_{SL}$ direction is present throughout the superlattice transformation, such that the NC AL orientation in the prealigned hexatic structure determines the orientation of the final square superlattice. During later stages of the assembly transformation, toward the unconnected square superlattice and prior to NC attachment, the NCs undergo a fine orientation alignment resulting in narrowed in-plane alignment distribution. We tested the generality of this interpretation by examining PbSe monolayer films using SAED. We confirmed the correlation along the $<11n>_{AL}$ and $<11>_{SL}$ and the decrease in AL misalignment as the superlattice transforms from hexatic to square. Finally, we found that monolayer superlattice transformation occurs gradually within a grain, rather than through nucleation and coherent propagation in grain boundaries. This work provides new insights into the coordination of $\sim 10^5$ NCs during superlattice transformation to enable the formation of micrometer-sized grains and conclude that controlling NC AL alignment in the preformed unconnected hexatic assembly is essential for obtaining long-range ordered films of connected NCs.

ASSOCIATED CONTENT

Supporting Information

The Supporting Information is available free of charge at https://pubs.acs.org/doi/10.1021/acs.nanolett.0c01579.

Nanocrystal synthesis, superlattice fabrication, and characterization; EMPAD data processing details and supplementary analysis; and illustration of general and specific superlattice transformation pathways, symmetry breaking in hexatic structure, and summary of superlattice structure transformation (PDF)

Movie S1 (MP4)

Movie S2 (MP4)

AUTHOR INFORMATION

Corresponding Author

Tobias Hanrath − *Robert F. Smith School of Chemical and Biomolecular Engineering, Cornell University, Ithaca, New York 14853, United States;* orcid.org/0000-0001-5782-4666; Email: th358@cornell.edu

Authors

Jessica Cimada daSilva − *Robert F. Smith School of Chemical and Biomolecular Engineering, Cornell University, Ithaca, New York 14853, United States;* orcid.org/0000-0002-8108-5557

Michelle A. Smeaton − *Department of Materials Science and Engineering, Cornell University, Ithaca, New York 14853, United States;* orcid.org/0000-0001-9114-1009

https://dx.doi.org/10.1021/acs.nanolett.0c01579
Nano Lett. 2020, 20, 5267−5274

Tyler A. Dunbar − *Robert F. Smith School of Chemical and Biomolecular Engineering, Cornell University, Ithaca, New York 14853, United States;* orcid.org/0000-0003-2971-5766
Yuanze Xu − *Robert F. Smith School of Chemical and Biomolecular Engineering, Cornell University, Ithaca, New York 14853, United States*
Daniel M. Balazs − *Robert F. Smith School of Chemical and Biomolecular Engineering, Cornell University, Ithaca, New York 14853, United States;* orcid.org/0000-0001-7597-043X
Lena F. Kourkoutis − *School of Applied and Engineering Physics and Kavli Institute at Cornell for Nanoscale Science, Cornell University, Ithaca, New York 14853, United States;* orcid.org/0000-0002-1303-1362

Complete contact information is available at: https://pubs.acs.org/10.1021/acs.nanolett.0c01579

Notes

The authors declare no competing financial interest.

■ ACKNOWLEDGMENTS

This work was primarily supported by the U.S. Department of Energy, Office of Basic Energy Sciences, under award number DE-SC0018026. Electron microscopy was performed in the Cornell Center for Materials Research supported by the NSF MRSEC program (DMR-1719875). The FEI Titan Themis 300 was acquired through NSF-MRI-1429155, with additional support from Cornell University, the Weill Institute, and the Kavli Institute at Cornell. J.A.C.S. acknowledges support from CAPES, Brazil (13159/13-5), the NSF (1803878), Professor Jian-Min Zuo at the University of Illinois for granting access to the EMAPS software, and Dr. Yu-Tsun Shao for his help using the software. M.A.S. acknowledges support from the NSF GRFP under award number DGE-1650441.

■ REFERENCES

(1) Boles, M. A.; Engel, M.; Talapin, D. V. Self-Assembly of Colloidal Nanocrystals: From Intricate Structures to Functional Materials. *Chem. Rev.* **2016**, *116* (18), 11220−11289.
(2) Damasceno, P. F.; Engel, M.; Glotzer, S. C. Predictive Self-Assembly of Polyhedra into Complex Structures. *Science* **2012**, *337*, 453−457.
(3) Nie, Z.; Petukhova, A.; Kumacheva, E. Properties and emerging applications of self-assembled structures made from inorganic nanoparticles. *Nat. Nanotechnol.* **2010**, *5* (1), 15−25.
(4) Kagan, C. R.; Lifshitz, E.; Sargent, E. H.; Talapin, D. V. Building devices from colloidal quantum dots. *Science* **2016**, *353* (6302), No. aac5523.
(5) Kagan, C. R.; Murray, C. B. Charge transport in strongly coupled quantum dot solids. *Nat. Nanotechnol.* **2015**, *10* (12), 1013−1026.
(6) Balazs, D. M.; Loi, M. A. Lead-Chalcogenide Colloidal-Quantum-Dot Solids: Novel Assembly Methods, Electronic Structure Control, and Application Prospects. *Adv. Mater.* **2018**, *30* (33), 1800082.
(7) Maiti, S.; Andre, A.; Banerjee, R.; Hagenlocher, J.; Konovalov, O.; Schreiber, F.; Scheele, M. Monitoring Self-Assembly and Ligand Exchange of PbS Nanocrystal Superlattices at the Liquid/Air Interface in Real Time. *J. Phys. Chem. Lett.* **2018**, *9* (4), 739−744.
(8) Bealing, C. R.; Baumgardner, W. J.; Choi, J. J.; Hanrath, T.; Hennig, R. G. Predicting nanocrystal shape through consideration of surface-ligand interactions. *ACS Nano* **2012**, *6* (3), 2118−2127.
(9) Baumgardner, W. J.; Whitham, K.; Hanrath, T. Confined-but-connected quantum solids via controlled ligand displacement. *Nano Lett.* **2013**, *13* (7), 3225−3231.
(10) Whitham, K.; Yang, J.; Savitzky, B. H.; Kourkoutis, L. F.; Wise, F.; Hanrath, T. Charge transport and localization in atomically coherent quantum dot solids. *Nat. Mater.* **2016**, *15* (5), 557−563.
(11) McCray, A. R. C.; Savitzky, B. H.; Whitham, K.; Hanrath, T.; Kourkoutis, L. F. Orientational Disorder in Epitaxially Connected Quantum Dot Solids. *ACS Nano* **2019**, *13* (10), 11460−11468.
(12) Evers, W. H.; Schins, J. M.; Aerts, M.; Kulkarni, A.; Capiod, P.; Berthe, M.; Grandidier, B.; Delerue, C.; van der Zant, H. S. J.; van Overbeek, C.; Peters, J. L.; Vanmaekelbergh, D.; Siebbeles, L. D. A. High charge mobility in two-dimensional percolative networks of PbSe quantum dots connected by atomic bonds. *Nat. Commun.* **2015**, *6*, 8195.
(13) Kalesaki, E.; Delerue, C.; Morais Smith, C.; Beugeling, W.; Allan, G.; Vanmaekelbergh, D. Dirac Cones, Topological Edge States, and Nontrivial Flat Bands in Two-Dimensional Semiconductors with a Honeycomb Nanogeometry. *Phys. Rev. X* **2014**, *4* (1), 011010.
(14) Kalesaki, E.; Evers, W. H.; Allan, G.; Vanmaekelbergh, D.; Delerue, C. Electronic structure of atomically coherent square semiconductor superlattices with dimensionality below two. *Phys. Rev. B: Condens. Matter Mater. Phys.* **2013**, *88* (11), 115431.
(15) Liu, Y.; Peard, N.; Grossman, J. C. Bandlike Transport in PbS Quantum Dot Superlattices with Quantum Confinement. *J. Phys. Chem. Lett.* **2019**, *10* (13), 3756−3762.
(16) Alimoradi Jazi, M.; Janssen, V.; Evers, W. H.; Tadjine, A.; Delerue, C.; Siebbeles, L. D. A.; van der Zant, H. S. J.; Houtepen, A. J.; Vanmaekelbergh, D. Transport Properties of a Two-Dimensional PbSe Square Superstructure in an Electrolyte-Gated Transistor. *Nano Lett.* **2017**, *17* (9), 5238−5243.
(17) Abelson, A.; Qian, C.; Salk, T.; Luan, Z.; Fu, K.; Zheng, J. G.; Wardini, J. L.; Law, M. Collective topo-epitaxy in the self-assembly of a 3D quantum dot superlattice. *Nat. Mater.* **2020**, *19* (1), 49−55.
(18) Geuchies, J. J.; van Overbeek, C.; Evers, W. H.; Goris, B.; de Backer, A.; Gantapara, A. P.; Rabouw, F. T.; Hilhorst, J.; Peters, J. L.; Konovalov, O.; Petukhov, A. V.; Dijkstra, M.; Siebbeles, L. D. A.; van Aert, S.; Bals, S.; Vanmaekelbergh, D. In situ study of the formation mechanism of two-dimensional superlattices from PbSe nanocrystals. *Nat. Mater.* **2016**, *15* (12), 1248−1254.
(19) Wang, Y.; Peng, X.; Abelson, A.; Xiao, P.; Qian, C.; Yu, L.; Ophus, C.; Ercius, P.; Wang, L.-W.; Law, M.; Zheng, H. Dynamic deformability of individual PbSe nanocrystals during superlattice phase transitions. *Science* **2019**, *5*, No. eaaw5623.
(20) Tate, M. W.; Purohit, P.; Chamberlain, D.; Nguyen, K. X.; Hovden, R.; Chang, C. S.; Deb, P.; Turgut, E.; Heron, J. T.; Schlom, D. G.; Ralph, D. C.; Fuchs, G. D.; Shanks, K. S.; Philipp, H. T.; Muller, D. A.; Gruner, S. M. High Dynamic Range Pixel Array Detector for Scanning Transmission Electron Microscopy. *Microsc. Microanal.* **2016**, *22* (1), 237−249.
(21) Ophus, C. Four-Dimensional Scanning Transmission Electron Microscopy (4D-STEM): From Scanning Nanodiffraction to Ptychography and Beyond. *Microsc. Microanal.* **2019**, *25* (3), 563−582.
(22) Bian, K.; Richards, B. T.; Yang, H.; Bassett, W.; Wise, F. W.; Wang, Z.; Hanrath, T. Optical properties of PbS nanocrystal quantum dots at ambient and elevated pressure. *Phys. Chem. Chem. Phys.* **2014**, *16* (18), 8515−8520.
(23) Zuo, J. M.; Mabon, J. C. Web-Based Electron Microscopy Application Software: Web-EMAPS. *Microsc. Microanal.* **2004**, *10* (S02), 1000−1001.
(24) Whitham, K.; Hanrath, T. Formation of Epitaxially Connected Quantum Dot Solids: Nucleation and Coherent Phase Transition. *J. Phys. Chem. Lett.* **2017**, *8* (12), 2623−2628.
(25) Weidman, M. C.; Nguyen, Q.; Smilgies, D.-M.; Tisdale, W. A. Impact of Size Dispersity, Ligand Coverage, and Ligand Length on the Structure of PbS Nanocrystal Superlattices. *Chem. Mater.* **2018**, *30* (3), 807−816.
(26) Weidman, M. C.; Smilgies, D. M.; Tisdale, W. A. Kinetics of the self-assembly of nanocrystal superlattices measured by real-time in situ X-ray scattering. *Nat. Mater.* **2016**, *15* (7), 775−781.

(27) Simon, P.; Bahrig, L.; Baburin, I. A.; Formanek, P.; Roder, F.; Sickmann, J.; Hickey, S. G.; Eychmuller, A.; Lichte, H.; Kniep, R.; Rosseeva, E. Interconnection of nanoparticles within 2D superlattices of PbS/oleic acid thin films. *Adv. Mater.* **2014**, *26* (19), 3042−3049.
(28) Novak, J.; Banerjee, R.; Kornowski, A.; Jankowski, M.; Andre, A.; Weller, H.; Schreiber, F.; Scheele, M. Site-Specific Ligand Interactions Favor the Tetragonal Distortion of PbS Nanocrystal Superlattices. *ACS Appl. Mater. Interfaces* **2016**, *8* (34), 22526−22533.
(29) van der Stam, W.; Rabouw, F. T.; Vonk, S. J.; Geuchies, J. J.; Ligthart, H.; Petukhov, A. V.; de Mello Donega, C. Oleic Acid-Induced Atomic Alignment of ZnS Polyhedral Nanocrystals. *Nano Lett.* **2016**, *16* (4), 2608−2614.
(30) Fan, Z.; Grunwald, M. Orientational Order in Self-Assembled Nanocrystal Superlattices. *J. Am. Chem. Soc.* **2019**, *141* (5), 1980−1988.
(31) Korgel, B. A.; Fitzmaurice, D. Small-angle x-ray-scattering study of silver-nanocrystal disorder-order phase transitions. *Phys. Rev. B: Condens. Matter Mater. Phys.* **1999**, *59* (22), 14191−14201.

https://dx.doi.org/10.1021/acs.nanolett.0c01579
Nano Lett. 2020, 20, 5267−5274